Quantitative evaluation of the reduction of distortion and metallic artifacts in magnetic resonance images using the multiacquisition variable-resonance image combination selective sequence

MASAKI HIRANO[1,2*], YUKI MUTO[1,3*], MASAHIRO KURODA[1*], YUTA FUJIWARA[4], TOMOAKI SASAKI[1,5], KAZUHIRO KURODA[1,6], RYO KAMIZAKI[1], SATOSHI IMAJOH[1], YOSHINORI TANABE[1], WLLA E. AL-HAMMAD[7], YUKI NAKAMITSU[1], YUDAI SHIMIZU[7], KOHEI SUGIMOTO[8], MASATAKA OITA[8], IRFAN SUGIANTO[9] and BABATUNDE O. BAMGBOSE[10]

[1]Department of Radiological Technology, Graduate School of Health Sciences, Okayama University, Okayama 700-8558; [2]Department of Radiology, Osaka Red Cross Hospital, Osaka 543-8555; [3]Department of Radiology, Oomoto Hospital, Okayama 700-0924; [4]Division of Clinical Radiology Service, Okayama Central Hospital, Okayama 700-0017; [5]Department of Diagnostic Radiology, National Cancer Center Hospital East, Chiba 277-8577; [6]Department of Health and Welfare Science, Graduate School of Health and Welfare Science, Okayama Prefectural University, Okayama 719-1197; [7]Department of Oral and Maxillofacial Radiology, Okayama University Graduate School of Medicine, Dentistry and Pharmaceutical Sciences, Okayama 700-0017; [8]Graduate School of Interdisciplinary Sciences and Engineering in Health Systems, Okayama University, Okayama, 770-8558, Japan; [9]Department of Oral Radiology, Faculty of Dentistry, Hasanuddin University, Makassar, Sulawesi 90245, Indonesia; [10]Department of Oral Diagnostic Sciences, Faculty of Dentistry, Bayero University, Kano 00234, Nigeria

Received October 5, 2022; Accepted January 4, 2023

DOI: 10.3892/etm.2023.11808

Abstract. Magnetic resonance imaging (MRI) is superior to computed tomography (CT) in determining changes in tissue structure, such as those observed following inflammation and infection. However, when metal implants or other metal objects are present, MRI exhibits more distortion and artifacts compared with CT, which hinders the accurate measurement of the implants. A limited number of reports have examined whether the novel MRI sequence, multiacquisition variable-resonance image combination selective (MAVRIC SL), can accurately measure metal implants without distortion. Therefore, the present study aimed to demonstrate whether MAVRIC SL could accurately measure metal implants without distortion and whether the area around the metal implants could be well delineated without artifacts. An agar phantom containing a titanium alloy lumbar implant was used for the present study and was imaged using a 3.0 T MRI machine. A total of three imaging sequences, namely MAVRIC SL, CUBE and magnetic image compilation (MAGiC), were applied and the results were compared. Distortion was evaluated by measuring the screw diameter and distance between the screws multiple times in the phase and frequency directions by two different investigators. The artifact region around the implant was examined using a quantitative method following standardization of the phantom signal values. It was revealed that MAVRIC SL was a superior sequence compared with CUBE and MAGiC, as there was significantly less distortion, a lack of bias between the two different investigators and significantly reduced artifact regions. These results suggested the possibility of utilizing MAVRIC SL for follow-up to observe metal implant insertions.

Correspondence to: Professor Masahiro Kuroda, Department of Radiological Technology, Graduate School of Health Sciences, Okayama University, 2-5-1 Shikata-cho, Kita-ku, Okayama 700-8558, Japan
E-mail: kurodamd@cc.okayama-u.ac.jp

*Contributed equally

Abbreviations: CT, computed tomography; FWHM, full width at half maximum; MAGiC, magnetic image compilation; MAVRIC SL, multiacquisition variable-resonance image combination selective; MRI, magnetic resonance imaging; SEMAC, slice-encoding for metal artifact correction; VAT, view-angle-tilting

Key words: MAVRIC SL, metal artifacts, implant, phantom, MRI

Introduction

Plain radiographs, computed tomography (CT), and magnetic resonance imaging (MRI) are routinely used in orthopedic imaging. Although there is some exposure to X-rays, plain radiographs are frequently used in daily clinical practice because of their low exposure dose, short time, and simplicity. CT is a three-dimensional imaging examination of the body's X-ray permeability and is used for the three-dimensional understanding and diagnosis of low permeability bone lesions,

and although it involves a certain amount of X-ray exposure, it is used for the diagnosis of bone lesions and postoperative observation because it provides detailed three-dimensional information. MRI is an examination that uses magnetic force to produce three-dimensional images of information obtained from hydrogen atoms in the body. Compared to CT, MRI provides detailed qualitative diagnostic information of soft tissues and is used to diagnose lesions such as inflammation and tumors. Since there is no exposure to x-rays, MRI can be used repeatedly and for follow-up (1).

In the field of orthopedic surgery, plain radiographs are the most commonly used imaging technique because of their simplicity, but they are two-dimensional images with little information, and the state of the soft tissues surrounding the bones cannot be grasped (1). Plain radiographs and CT have the advantage of superior bone diagnosis, but have the disadvantage of exposure to X-rays. MRI has the advantage of being superior in diagnosing periosteal inflammation and tumors (2), but has the disadvantage of being inferior to CT in diagnosing the bone itself. Besides, the disadvantage of MRI is the distortion and potent artifacts caused by the presence of metal in the body (3).

The advantage of MRI compared with X-ray and CT images (2) is the high contrast of the normal structures in soft tissues and lesions, such as those observed during inflammation and tumor formation. However, a disadvantage of MRI compared with other imaging techniques is the distortion and evident artifacts caused by the presence of metal in the body (3).

In recent years, the surgical demand for spinal compression fractures has increased due to an aging population, and therefore orthopedic lumbar implants have become increasingly popular. Following the insertion of a metal implant, it is necessary to accurately ascertain the state of the insertion. Currently, CT, which has less distortion in general, is used more frequently than MRI for 3D imaging. However, infections and hematoma may occur at the insertion site following implantation (3). MR images are more useful than radiographs or CT images for evaluations of infections and hematoma (4,5). Therefore, MRI methods are continuously developed to reduce artifacts from metallic implants, as these are considered to hinder certain diagnoses.

One of these MRI methods is the multiacquisition variable-resonance image combination (MAVRIC). MAVRIC is a method of synthesizing off-resonant frequency information in the metallic environment by acquiring various high-frequency offsets. MAVRIC selective (MAVRIC SL) is a combination of MAVRIC and slice-encoding for metal artifact correction (SEMAC) (3,6). SEMAC is a method for correcting in-plane distortions by applying the view-angle-tilting (3,7,8) technique, in which the acquisition slice selection gradient is corrected by the readout gradient (9). A limited number of reports have investigated the ability of MAVRIC SL to accurately measure metal implants without distortion (10). Most of the reports on the reduction of the metal artifacts with the MAVRIC SL are based on visual and qualitative methods, and only a limited number of reports have investigated the quantitative methods (10).

Therefore, the present study aimed to quantitatively evaluate the effectiveness of MAVRIC SL (11) in reducing the distortion and metal artifacts of lumbar implants. The present study is also fairly novel in its use of phantom experiments to clarify the useful application of MAVRIC SL.

Materials and methods

Preparation of implant-embedded phantom. An agar phantom (Fig. 1A) with a titanium implant was prepared. A plastic implant support was placed inside a 280x190x145 mm plastic container. A titanium alloy lumbar implant (5.5/6.0 mm CD Horizon™ Solera™ with a 7.5x40 mm Cannulated Multi-Axial Screw; Medtronic Sofamor Danek, Co., Ltd.) was placed on the support base. Three screws were fixed to one rod. The minor diameter, which is the diameter of the screw excluding the threads, was 5.5 mm, whereas the nominal diameter, which is the diameter including the threads, was 7.5 mm. The two rods were placed in parallel. The vessel was filled with agar, which was used at a final concentration of 0.8% (w/w), and dissolved in 0.9% saline.

Imaging, post-processing and CT imaging. A 64 multi-row detector CT (Sensation 64; Siemens AG) was used. The imaging parameters were as follows: Tube voltage 140 kVp, automated tube current modulation, collimation 0.6x64 mm, and helical pitch 32. A coronal section image of the phantom was reconstructed with a reconstruction matrix of 512x512 and a slice thickness of 2 mm.

MRI. 3.0 T SIGNA Architect ver. 26.1, Posterior Array Coil and Anterior Array Coil (GE) were used. MAVRIC SL, CUBE and magnetic image compilation (MAGiC) were used as a metal artifact reduction sequence, a 3D fast spin-echo sequence and a synthetic MRI sequence, respectively. The coronal section images of the phantom were obtained using the imaging parameters in Table I.

Unification of image resolution. The different resolutions of CT and MRI images were included using the image analysis software MATLAB 2020a (MathWorks Inc.). The resolution of each MRI image was converted to 512x512 to match the maximum resolution of the CT without altering the pixel signal values.

Quantitative measurement of screws and evaluation methods Measurement of the screw diameter (SCD) and the distance between the screws (DBSC). Concerning the methodology for the evaluation of SCD and DBSC, using the image in which the screws are depicted, a straight line overlapping the screws was drawn, and a profile curve of the signal value on the line was obtained. The constant changing part of the signal value in the profile curve was defined as the screw part, and SCD and DBSC were quantitatively measured. More specifically, SCD and DBSC were measured and evaluated as a distortion using MATLAB; the CT and MR images of the coronal sections were estimated as shown in Fig. 1B. Five slices with the same depth in the CT and MR images were selected for each measurement. The measurement directions are the horizontal directions shown in columns a, b and c and the vertical directions are those indicated in columns d and e (Fig. 1C). The horizontal and vertical directions correspond to the phase and

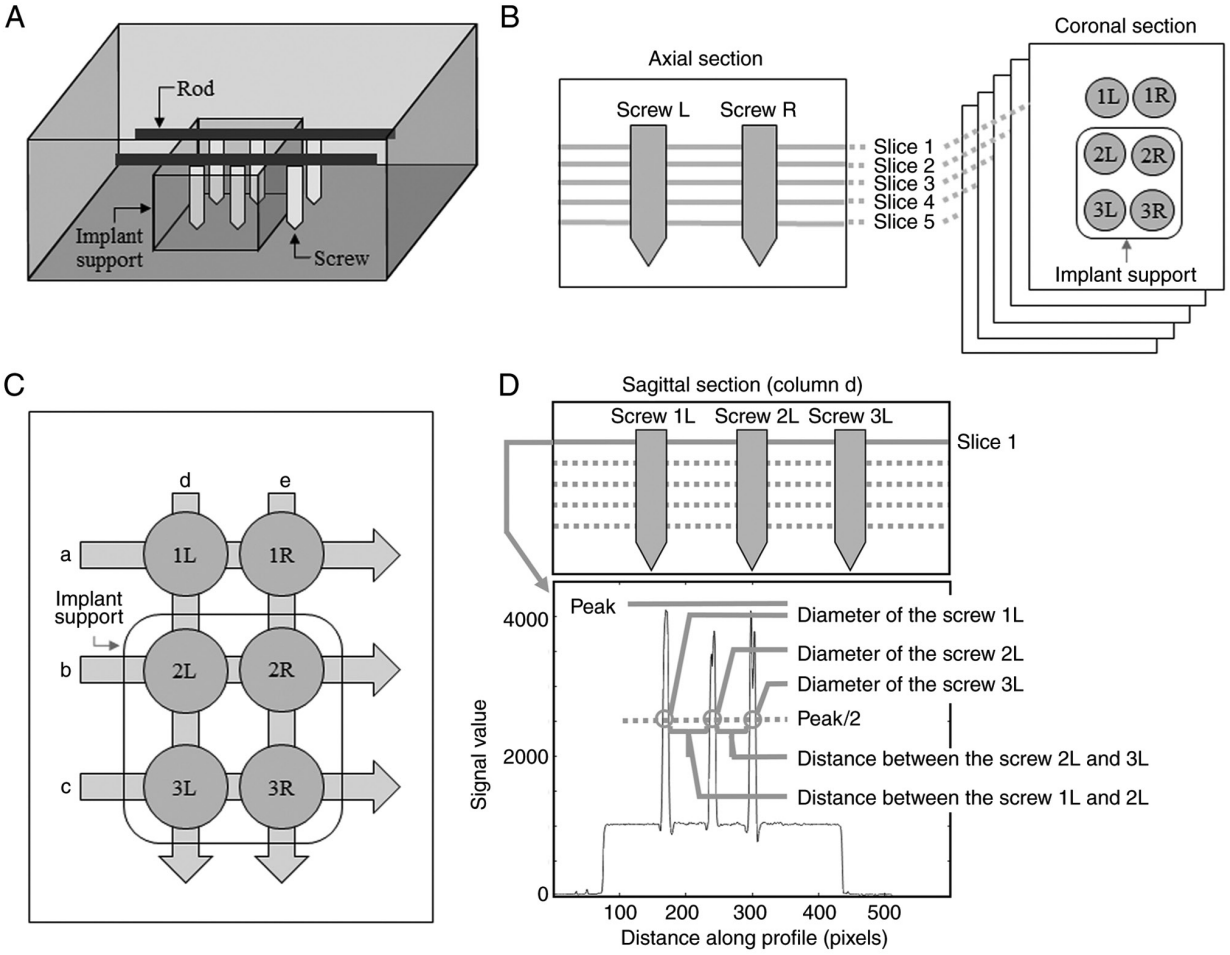

Figure 1. Measurement of the screw diameter and the distance between the screws. (A) Overall view of a titanium implant-embedded agar phantom. (B) Selection of five slices for the measurement of the CT and MRI images. (C) The direction of the five columns of the measurements in each slice. (D) Example of the measurement of the screw diameter and the distance between the screws using the FWHM value for the profile curve of column d in (C). CT, computed tomography; MRI, magnetic resonance imaging; FWHM, full width at half maximum.

frequency directions in the MRI method, respectively. Fig. 1D indicates the measurement of column d (Fig. 1C) in the CT image. Column d with 1L, 2L and 3L screws was selected. A profile curve was plotted with the signal value of column d on the vertical axis and the pixel number of column d on the horizontal axis. The diameters of the 1L, 2L, and 3L screws were quantitatively measured as the full width at half maximum (FWHM) of the mountainous spread of the signal values. DBSC was quantitatively measured as the distance between two FWHM values. These parameters were also measured in the same way using MR images. Two separate investigators measured a total of nine locations for each of the five slices, six screws and three DBSCs for the horizontal direction. With regard to the vertical direction, six locations were measured for each of the four screws (2L, 3L, 2R and 3R) and the two DBSCs were measured to avoid the influence of the implant support. Two investigators repeated these measurements three times each, one week apart.

Evaluation of SCD and DBSC. The enlargement index of SCDs and DBSC in the images of the three MR sequences were compared with those measured in the CT images. The assessment was performed using the magnification ratio as indicated in equation 1:

Magnification ratio=Measurements in MRI/Measurements in CT

The magnification ratio of SCD was measured for each screw. In the phase direction, a total of 180 magnification ratios were calculated (six screws and five slices, each measured thrice by two investigators). In the frequency direction, a total of 120 magnification ratios were calculated (four screws and five slices, each measured thrice by two investigators). Subsequently, the median, lower quartile (q1) and upper quartile (q3) of each magnification ratio were calculated.

The magnification ratio of each DBSC was also measured. In the phase direction, a total of 90 magnification ratios were calculated (three DBSCs and five slices, each measured thrice by two investigators). In the frequency direction, a total of 60 magnification ratios were calculated (two DBSCs and five slices, each measured thrice by two investigators). Then, the median, q1 and q3 of each of these magnification ratios were also calculated.

Evaluation of measurement bias between the investigators performing the measurements. Concerning the evaluation of measurement of bias between the investigators performing the measurements, the fixed and proportional biases were

Table I. MR sequences.

Parameters	MAGiC	CUBE	MAVRIC SL
TR/TE, msec	4,000-5,600/23-95	3,000/13	3,000/6.3
FOV, mm	300x300	300x300	300x300
Matrix size	320x192	320x320	256x256
Slice thickness, mm	1.8	0.9	1.4
Number of slices	32	76	38
Flip angle, °	NA	NA	60
ARC	Phase: 2.25	Phase: 2.5 Slice: 2.0	Phase: 3.0 Slice: 2.0
ETL	16	60	20
Phase direction	L/R	L/R	L/R
Frequency direction	S/I	S/I	S/I
Echo spacing, msec	10.0	4.7	6.3
Band width, Hz/pixel	156.2	488.3	976.6
Scan time, min:sec	4:51	5:10	5:06

MAGiC, magnetic resonance image compilation; MAVRIC SL, multiacquisition variable-resonance image combination selective; TR, repetition time; TE, echo time; MDME, multi-delay multi echo; FOV, field of view; ARC, autocalibrating reconstruction for Cartesian imaging; ETL, echo train length; L/R, left-right; S/I, superior-inferior.

used (12,13). The fixed biases are errors that are biased in a certain direction, regardless of the true value. The proportional biases are errors that are in a certain direction in proportion to the true value. The fixed biases were evaluated statistically using the difference between the two investigators. The proportional biases were evaluated by the Bland-Altman plot, using the mean and difference between the two investigators. Specifically, the fixed and proportional biases of the measurements performed between the two investigators were evaluated. The fixed bias of SCDs and the difference between SCDs measured by the two investigators were calculated for each screw. In the phase direction, a total of 90 differences were calculated for six screws, five slices and three measurements. In the frequency direction, a total of 60 differences were calculated for four screws, five slices and three measurements. Subsequently, the median, q1 and q3 of each difference were calculated.

The fixed bias of DBSC was assessed as follows: The difference between DBSC was measured by the two investigators (one for each DBSC). In the phase direction, a total of 45 differences were calculated for three DBSCs, five slices and three measurements. In the frequency direction, a total of 30 differences were calculated for two DBSCs, five slices and three measurements. Subsequently, the median, q1 and q3 of each difference were calculated.

Bland-Altman plots were used to determine the proportional bias. The presence or absence of a correlation between the difference and the mean in SCDs, as well as DBSC, between the two investigators was examined (12,13).

Quantitative evaluation of artifacts in MR images (Fig. 2)
Selection of slices for evaluation. RadiAnt DICOM Viewer (64-bit; XLsoft Corporation) was used. For image analysis, one slice at the central level of the depth of the phantom was extracted from the coronal section MR images of each sequence. This slice was selected since SCD was constant and suitable for analysis at this level.

Creation of standardized images (Fig. 2). Standardization is a preprocessing method for comparing different data (Data transformation; https://www.kdnuggets.com/2020/04/data-transformation-standardization-normalization.html). In this study, standardized images were created to compare images taken in three different sequences (Fig. 3). The standardized images show how far the signal value of each image is from the average value of each image. Standardization was performed only for MR images and not for CT images. Concretely, for the MR image of each sequence, the signal value of each pixel of the entire slice was standardized using the signal value of the phantom in the artifact-free region. The image created using the standardized signal values was defined as the standardized image. A phantom region of interest (ROI; Fig. 3B) was used to extract the artifact-free region in the phantom image. The phantom ROI is the region from which the central portion and the phantom edges are removed from the entire phantom. The central portion is the part where the metal artifacts are noted around the six screws and the phantom edges are the parts where the signal values are unstable. The mean, standard deviation of the signal values within the phantom ROI, and the following equation (equation 2) were used to calculate the standardized signal values:

Standardized signal value=(signal value-mean value of phantom ROI)/standard deviation of phantom ROI

The purpose of establishing standardized images is to quantitatively compare the differences in the signal values of the artifact region in the MR images of each sequence with

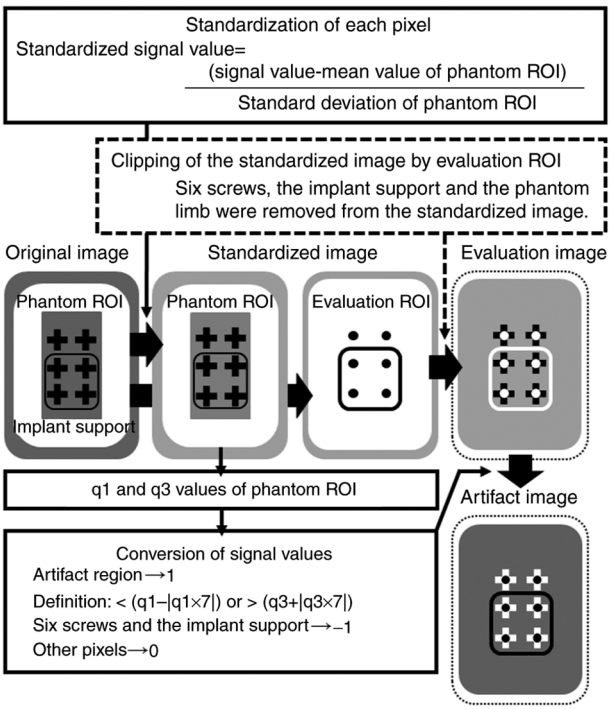

Figure 2. The process of quantitative evaluation of artifacts in MR images. Cross symbols indicate artifact regions. The white 'phantom ROIs' were used to create the standardized image and to define the artifact region by q1 and q3. The white 'evaluation ROI' indicates the phantom evaluation ROI, which was used to create the evaluation image. ROI, region of interest; MR, magnetic resonance; q1, lower quartile; q3, upper quartile.

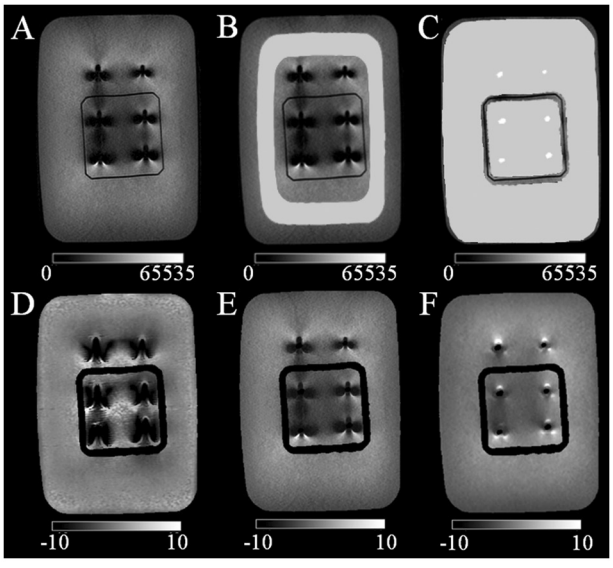

Figure 3. ROI settings and evaluation images. (A) MR image of CUBE. (B) Phantom ROI. The range of the phantom ROI is shown in light gray for the MR image of (A). (C) Evaluation of ROI. The range of the evaluation of ROI is shown in light gray for the MR image of (A). The regions of the screws (white) and the implant support (black) are not included in the evaluation of the ROI. (D) Evaluation image of MAGiC. (E) Evaluation image of CUBE. (F) Evaluation image of MAVRIC SL. The scale bars at the bottom of the images indicate the range of signal values of each image. ROI, region of interest; MR, magnetic resonance; MAGiC, magnetic image compilation.

the same distribution of signal values in the phantom of the artifact-free regions.

Generation of evaluation images (Fig. 2). To quantitatively evaluate the regions of the metal artifacts, an evaluation image (Fig. 3D-F) was constructed using standardized images from each sequence. The evaluation image was defined as the image from which the region of the phantom evaluation ROI (Fig. 3C) was extracted from the standardized image. The phantom evaluation ROI is the region from which the regions of six screws and the implant support are removed from the entire phantom. The regions of the six screws were determined using the CT image with little or no metal artifact.

Quantitative evaluation of artifact regions in the images (Fig. 2). Regions of signal values that deviated from a certain signal value based on standardized images were defined as artifact regions (Fig. 3). More specifically, the artifact region in the evaluation image was defined using the q1 and q3 of the signal values of all pixels in the phantom ROI of the standardized image. An artifact region was defined as a region where the signal value was <(q1-|q1x7|) or >(q3+|q3x7|). In general, outliers were defined as the range where the signal value was <(q1-|q1xX|) or the range where the signal value was >(q3+|q3xX|). In the present study, the constant 'X' was determined as the value at which the defined artifact region visually matched the artifact region in the standardized image (data not shown).

Construction of artifact images (Fig. 2). Artifact images were created by replacing the signal value of an artifact region with a certain value and replacing other regions with another constant value (Fig. 3). In the evaluation of artifact regions, the percentage of artifact regions in the artifact images of different sequences was quantitatively compared. More specifically, the artifact images were constructed based on the evaluation images following these steps: i) The signal values of all pixels that fitted the definition of an artifact region were converted to 1; ii) the signal values of the pixels in the region of the six screws and the implant support were converted to -1; and iii) the signal values of all other pixels were converted to 0.

Statistical analysis. SPSS (version 25; SPSS, Inc.) was used for statistical processing. For the examination of the magnification ratio and fixed biases, the medians, q1 and q3 were used, since the Shapiro-Wilk test revealed the absence of normality in the measurement data (data not shown). Non-parametric Kruskal-Wallis with a Dunn test was used to assess the significant differences among the MR sequences. The examination of proportional bias was performed using the Spearman's correlation coefficient rs value between the differences. Moreover, the mean of the measurements of the two investigators was calculated, since the Shapiro-Wilk test revealed the absence of normality in the measurement data (data not shown). Fisher's Z-transformation was used to assess the significant differences in the rs values between the MR sequences.

In the evaluation of artifact regions, the ratio of the number of pixels in the artifact region of each MR sequence to the total number of pixels in the remaining part of the phantom was compared by multiple χ^2 tests with a Bonferroni correction. $P<0.05$ was considered to indicate a statistically significant difference.

Table II. The magnification ratio to CT.

Direction	Measured object of the magnification ratio	MR sequences		
		MAGiC	CUBE	MAVRIC SL
Phase	Screw diameter	3.24[a] (2.92, 3.75)	3.44[a] (3.09, 4.18)	1.88 (1.61, 2.45)
	Distance between the screws	0.73[a] (0.62, 0.78)	0.64[a] (0.62, 0.71)	0.86 (0.85, 0.89)
Frequency	Screw diameter	3.53[a,b] (3.05, 3.97)	2.81[a,c,d] (2.60, 3.06)	1.41[c] (1.25, 1.65)
	Distance between the screws	0.58[a,c] (0.51, 0.65)	0.70[a,c,d] (0.66, 0.72)	0.87 (0.82, 0.90)

Data are shown as the median (upper quadrant, lower quadrant) of the ratios of length on MRI to length on CT. [a]Significantly difference compared to MAVRIC SL, P<0.05 by Kruskal-Wallis with a Dunn test; [b]Significantly difference compared to phase direction, P<0.05 by Kruskal-Wallis with a Dunn test; [c]Significantly difference compared to phase direction, P<0.001 by Kruskal-Wallis with a Dunn test; [d]Significantly difference compared to MAGiC, P<0.05 by Kruskal-Wallis with a Dunn test.

Table III. Difference between measurements of two investigators; analysis of fixed bias.

Direction	Measured object	MR sequences		
		MAGiC	CUBE	MAVRIC SL
Phase	Screw diameter, mm	0 (-1.172, 1.172)	0 (-0.586, 0)	0 (-0.172, 0)
	Distance between the screws, mm	0 (-1.172, 1.172)	0.586 (0, 0.586)	0 (0, 1.172)
Frequency	Screw diameter, mm	0[a] (0, 1.172)	0 (-0.586, 1.172)	0 (-1.172, 0)
	Distance between the screws, mm	0 (-0.586, 1.172)	-0.586[a] (-1.172, 0.586)	0 (0, 1.172)

Data are shown as the median (upper quadrant, lower quadrant) of the difference between measurements of two investigators. [a]Significant difference compared to MAVRIC SL, P<0.05 by Kruskal-Wallis with a Dunn test.

Results

Magnification ratio of SCD and DBSC to CT. In the CT images, the median SCD (q1, q3) was 5.0 (4.4, 6.3) mm for the horizontal measurements, 5.0 (4.4, 5.6) mm for the vertical measurements and 5.0 (4.4, 5.6) mm for the overall measurements. Table II indicates the magnification ratio of SCD and DBSC to CT for each sequence of the MR images. The MAVRIC SL exhibited the lowest measurement error compared with that of the other MR sequences; the magnification of SCD and DBSC were significantly closer to 1 in both phase and frequency directions (MAVRIC SL vs. MAGiC, CUBE; P<0.05). Concerning the magnification ratio of SCD and DBSC to CT, ratios ranged from 0.58-0.73 and 2.81-3.44 for the MAGiC and CUBE, with a large difference from 1.

The comparison of the phase and frequency directions demonstrated that the magnification ratios of SCD in the frequency direction approached 1 (P<0.001) for CUBE and MAVRIC SL with a limited measurement error. In MAGiC, the magnification ratio of SCD was significantly >1 in the frequency direction compared with that in the phase direction, and the measurement error was higher. In MAGiC, the magnification ratio of DBSC was significantly <1 in the frequency direction than that noted in the phase direction, and the measurement error was higher. In CUBE, the magnification ratio of DBSC in the frequency direction approached 1 (P<0.05) compared with that noted in the phase direction, with a lower measurement error.

Measurement bias. Table III indicates the fixed biases. In all measurements, the median value of difference between two investigators approached zero and the fixed biases were small. For the frequency direction, significant differences were found in SCD of MAGiC and in DBSC of CUBE compared with those of MAVRIC SL as determined by the Kruskal-Wallis with a Dunn test (P<0.05). Table IV indicates the proportional biases. No proportional biases were found for the MAVRIC SL. In the phase direction, a correlation was observed in SCD obtained by MAGiC and in that obtained by CUBE. Fisher's Z-transformation revealed significant differences in the rs values of SCDs between the CUBE and MAGiC sequences (P=0.0001) and in SCDs between the MAVRIC SL and MAGiC sequences (P=0.0042). In the frequency direction, a correlation was found in DBSC of MAGiC. The differences in the rs values of DBSC were significant as determined by Fisher's Z-transformation (P=0.0005) following the comparison between MAVRIC SL and MAGiC.

Evaluation of artifact regions. Fig. 4A indicates the histograms of the signal values in the evaluation images for each sequence. A low number of differences are noted in the distribution of the signal values in the phantom evaluation ROI among sequences due to the standardization. The spread of the distribution of the signal values outside the phantom evaluation ROI was lower in MAVRIC SL (Fig. 4Ac) compared with that in the MAGiC (Fig. 4Aa) and CUBE sequences (Fig. 4Ab). Table V

Table IV. Correlation between difference and average of measurements of two investigators; analysis of proportional bias.

Direction	Measured object	MR sequences		
		MAGiC	CUBE	MAVRIC SL
Phase	Screw diameter	0.30[a]	-0.28[a,b]	-0.12[c]
	Distance between the screws	-0.1	-0.08	0.06
Frequency	Screw diameter	-0.07	0.02	0
	Distance between the screws	-0.61[a]	-0.2	0.24[d]

Data are presented as Spearman's rank correlation coefficient, rs ([a]P<0.01). Significant difference compared to MAGiC by Fisher's Z-transformation ([b]P=0.0001, [c]P=0.0042, [d]P=0.0005).

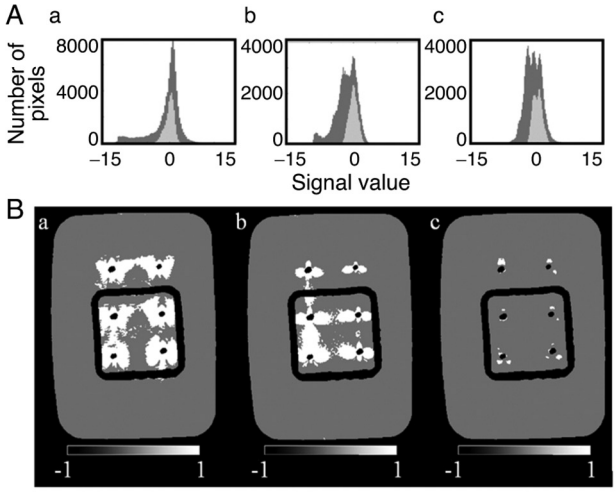

Figure 4. Histogram of the evaluation and artifact images. (A) Histogram of the evaluation image. (a) MAGiC, (b) CUBE, and (c) MAVRIC SL. The light gray color indicates the signal values of the pixels in the phantom ROI and the dark gray color indicates the signal values of the pixels used in the evaluation of ROI. (B) Artifact images. (a) MAGiC, (b) CUBE, and (c) MAVRIC SL. The white color indicates the defined artifact regions, whereas the gray color indicates the phantom regions and the black color indicates the regions of the screws, the implant support, and the background. MAGiC, magnetic image compilation; MAVRIC SL, multiacquisition variable-resonance image combination selective.

Table V. Signal values of pixels in the phantom ROI for each MR evaluation image and definition of the artifact region.

MR images	Signal values	
	Phantom ROI	Definition of artifact region
MAGiC	0.141 (-0.558, 0.700)	<-4.602, >5.603
CUBE	0.017 (-0.676, 0.684)	<-5.404, >5.472
MAVRIC SL	0.012 (-0.771, 0.726)	<-6.170, >5.808

ROI, region of interest. Data are shown as the median (upper quadrant, lower quadrant) of signal values in the phantom ROI. The artifact region is defined by calculation using signal values of upper and lower quadrants in phantom ROI.

Table VI. Comparison of artifacts for each MR sequence.

Sequence	Number of pixels (%)	
	Artifact region	Non-artifact region
MAGiC	11,489 (13.0)[a]	77,262 (87.0)[a]
CUBE	6,946 (7.8)[a]	81,805 (92.2)[a]
MAVRIC SL	484 (0.5)[a]	88,267 (99.5)[a]

[a]P<0.05 by multiple χ^2 tests with Bonferroni correction.

indicates the signal values of the pixels in the phantom ROI; the range of the signal values of the artifact region was defined by equation 2 for each sequence. The artifact images for each sequence prepared by this equation are shown in Fig. 4B. The artifact regions exhibited the following order: MAVRIC SL<CUBE<MAGiC.

Table VI indicates the quantitative evaluation of the artifact regions. The ratio of the pixels in the artifact region to the entire phantom exhibited the following order: MAVRIC SL<CUBE<MAGiC. For MAVRIC SL, the percentage of artifacts was as low as 0.5%. Multiple χ^2 tests with Bonferroni correction indicated a significant difference (P<0.05) in the percentage of the artifact regions among the sequences.

Discussion

The present study indicated that the magnification of MAVRIC SL was significantly lower than that noted for CUBE and MAGiC with regard to the measurements of SCD and DBSC for both phase and frequency directions. The bias between the two investigators was not observed. The MAVRIC SL was more useful than the CUBE and MAGiC sequences in accurately measuring implants and reducing distortion, with the quantitatively narrower area of artifacts around the implant.

Only one previous study (10) has examined the accuracy of implant geometry and measurement with the MAVRIC SL as a reduction in distortion. To the best of our knowledge, our previous study (10) was the first to report on this topic and only the phase direction was examined. In the present study, in addition to the phase direction, the frequency direction was also examined. In addition, the number of measurements was

increased from one (10) to three to increase the reliability of the measurements. In the present study, the accuracy of the implant measurement in the phase direction with the MAVRIC SL was as high as that noted in the previous study (10). The accuracy of the MAVRIC SL implant measurements in the frequency direction was significantly higher than that in the phase direction. The present study revealed that the measurement bias was reduced by selecting MAVRIC SL, probably because the magnification rate of MAVRIC SL was smaller than that of other sequences, and the absolute value of the error between the two investigators became smaller (10).

A significant number of studies have been reported in clinical practice (14-18) examining the extent of artifacts around the implant by MAVRIC SL. The present study is the first report to demonstrate in a quantitative manner, by using phantom experiments, that MAVRIC SL exhibits significantly reduced artifacts compared with that noted in other sequences. Various methods have been proposed to reduce the metal artifacts in MRI (3). Several reports have evaluated in a visual and qualitative manner that MAVRIC SL (8), which combines MAVRIC and SEMAC, reduces artifacts. Kretzschmar *et al* (18) compared MAVRIC SL with fast spin echo short tau inversion recovery in patients following hip implantation and reported reduced metal artifacts with MAVRIC SL. Liebl *et al* (17) reported that MAVRIC SL decreased the metal artifacts in the knee lesions. In our previous report (10), the data indicated in a qualitative way that the MAVRIC SL exhibited the narrower area of artifacts. The present study confirmed these results using a quantitative evaluation method. Gutierrez *et al* (14) evaluated MAVRIC SL and 2D-fast spin echo in a semi-quantitative way and reported the narrower area of metal artifacts in the MAVRIC SL.

Until recently, the MAVRIC SL could only be used in limited sequences with short echo times. Recent upgrades to the MAVRIC SL have made it possible to image T2-weighted images with long echo times. It is expected that inflammation, abscess formation and fluid retention in the vicinity of metallic implants will be evaluated in the future. To the best of our knowledge, a limited number of clinical reports have been published on T2-weighted images of MAVRIC SL; these results have to be further addressed in future studies (19,20). To improve the long acquisition time of the MAVRIC SL, a novel technique using robust principal component analysis has been developed, which has been reported to reduce metal artifacts and significantly shorten the scan time (21-23).

The first limitation of the present study was that the MR images were evaluated based on the CT images. The minor diameter of the screws used in the present study, which corresponds to the diameter of the screw excluding the threads, was 5.5 mm. The nominal diameter, which corresponds to the diameter including the threads, was 7.5 mm. In both CT and MR images, the body diameter was imaged considering a portion of the screw threads due to partial volume effects. The CT and MRI data were compared since the effects of the partial volume and those of the FWHM-based measurement method were similar for the two imaging methods. Although the appearance of the metal artifacts is also a limitation in the CT method, the diameter of the screw measured by CT in the present study was 5.0 (4.4-5.6) mm, which was considered to be within the acceptable range for the degree of measurements including the artifacts. Secondly, the artifacts in the imaging of the MAVRIC SL used in the present study were evaluated using proton density-weighted images with short echoes. T2-weighted images are preferable for clinical applications by detecting lesions, such as abscesses and hematomas, around metal implants. Our research group aims to conduct a study with a similar design when T2-weighted MAVRIC SL images (24), which are expected to be developed and widely used in the future, become available for routine clinical use (25). Finally, the present study used a phantom experiment, and future clinical studies that directly measure metal implants inserted into patients' bodies may need to be considered to conclude whether the results of the present study are clinically useful (26).

In conclusion, MAVRIC SL exhibited reduced implant measurement error, reduced bias between the two investigator measurements and the narrower area of artifacts around the implant compared with those noted in the CUBE and MAGiC methods. Among the MR imaging methods that can detect the tissue and lesions around metallic devices, MAVRIC SL was found to be a superior sequence with predominantly reduced artifacts on MR images compared with CUBE and MAGiC; moreover, to accurately measure screws and reduce measurement bias, it is preferable to use the MAVRIC SL rather than the CUBE or MAGiC for imaging implants.

Acknowledgements

The authors would like to thank Mr. Kaito Murakami, Mr. Yutaka Fujibuchi, Ms. Nao Ueda, Ms. Nayu Ohmukai and Mr. Naoya Miura of Okayama University (Okayama, Japan) for their assistance in analyzing the data.

Funding

The present study was supported by the Grant-in-Aid for Scientific Research (grant no. 19K0809801) from the Ministry of Health, Labour and Welfare of Japan.

Availability of data and materials

The datasets used and/or analyzed during the current study are available from the corresponding author on reasonable request.

Authors' contributions

MH, YM and MK participated in research design. MH, YM, YF, TS, RK, SI, YT, WEA, YN and YS performed the experiments and collected data. MH, YM and MK analyzed the data and were major contributors in writing the manuscript. KK, KS, MO, IS and BOB analyzed data and confirm the authenticity of all the raw data. All authors read and approved the final manuscript.

Ethics approval and consent to participate

Not applicable.

Patient consent for publication

Not applicable.

Competing interests

The authors declare that they have no competing interests.

References

1. Kreel L: Medical Imaging. Postgrad Med J 67: 334-346, 1991.
2. Elliott MJ and Slakey JB: CT provides precise size assessment of implanted titanium alloy pedicle screws. Clin Orthop Relat Res 472: 1605-1609, 2014.
3. Jungmann PM, Agten CA, Pfirrmann CW and Sutter R: Advances in MRI around metal. J Magn Reson Imaging 46: 972-991, 2017.
4. Smith MR, Artz NS, Wiens C, Hernando D and Reeder SB: Characterizing the limits of MRI near metallic prostheses. Magn Reson Med 74: 1564-1573, 2015.
5. Cyteval C and Bourdon A: Imaging orthopedic implant infections. Diagn Interv Imaging 93: 547-557, 2012.
6. Lu W, Pauly KB, Gold GE, Pauly JM and Hargreaves BA: Slice encoding for metal artifact correction with noise reduction. Magn Reson Med 65: 1352-1357, 2011.
7. Butts K, Pauly JM and Gold GE: Reduction of blurring in view angle tilting MRI. Magn Reson Med 53: 418-424, 2005.
8. Viano AM, Gronemeyer SA, Haliloglu M and Hoffer FA: Improved MR imaging for patients with metallic implants. Magn Reson Imaging 18: 287-295, 2000.
9. Bhoil A, Caw H and Vinjamuri S: Role of 18F-flurodeoxyglucose in orthopaedic implant-related infection: Review of literature and experience. Nucl Med Commun 40: 875-887, 2019.
10. Fujiwara Y, Sasaki T, Muto Y, Hirano M, Kamizaki R, Murakami K, Miura N, Fujibuchi Y, Ohmukai N, Ueda N, *et al*: Multiacquisition variable-resonance image combination selective can improve image quality and reproducibility for metallic implants in the lumbar spine. Acta Med Okayama 75: 187-197, 2021.
11. Koch KM, Brau AC, Chen W, Gold GE, Hargreaves BA, Koff M, McKinnon GC, Potter HG and King KF: Imaging near metal with a MAVRIC SL-SEMAC hybrid. Magn Reson Med 65: 71-82, 2011.
12. Hilson A: Bland-Altman plot. Radiology 231: 604; author reply 604-5, 2004.
13. Chen CP and Lin YM: Bland-Altman plots and receiver operating characteristic curves are preferred. Radiology 257: 896; author reply 896-7, 2010.
14. Gutierrez LB, Do BH, Gold GE, Hargreaves BA, Koch KM, Worters PW and Stevens KJ: MRI near metallic implants using MAVRIC SL: Initial clinical experience at 3T. Acad Radiol 22: 370-379, 2015.
15. Choi S, Koch MK, Hargreaves AB, Stevens JK and Gold EG: Metal artifact reduction with MAVRIC SL at 3-T MRI in patients with hip arthroplasty. AJR Am J Roentgenol 204: 140-147, 2015.
16. Hayter LC, Koff FM, Shah P, Koch MK, Miller TT and Potter GH: MRI after arthroplasty: Comparison of MAVRIC and conventional fast spin-echo techniques. AJR Am J Roentgenol 197: W405-W411, 2011.
17. Liebl H, Heilmeier U, Lee S, Nardo L, Patsch J, Schuppert C, Han M, Rondak IC, Banerjee S, Koch K, *et al*: In vitro assessment of knee MRI in the presence of metal implants comparing MAVRIC-SL and conventional fast spin echo sequences at 1.5 and 3 T field strength. J Magn Reson Imaging 41: 1291-1299, 2015.
18. Kretzschmar M, Nardo L, Han MM, Heilmeier U, Sam C, Joseph GB, Koch KM, Krug R and Link TM: Metal artifact suppression at 3 T MRI: Comparison of MAVRIC SL with conventional fast spin echo sequences in patients with hip joint arthroplasty. Eur Radiol 25: 2403-2411, 2015.
19. Ai T, Padua A, Goerner F, Nittka M, Gugala Z, Jadhav S, Trelles M, Johnson RF, Lindsey RW, Li X and Runge VM: SEMAC-VAT and MSVAT-SPACE sequence strategies for metal artifact reduction in 1.5T magnetic resonance imaging. Invest Radiol 47: 267-276, 2012.
20. Ariyanayagam T, Malcolm PN and Toms AP: Advances in metal artifact reduction techniques for periprosthetic soft tissue imaging. Semin Musculoskelet Radiol 19: 328-334, 2015.
21. Albakheet SS, Lee HY, Hahn S, Song TH, Suh SJ and Kaushik S: Accelerated metallic artifact reduction imaging using spectral bin modulation of multiacquisition variable-resonance image combination selective imaging. Magn Reson Imaging 72: 19-24, 2020.
22. Doyle Z, Yoon D, Lee KP, Rosenberg J, Hargreaves AB, Beaulieu FC and Stevens JK: Clinical utility of accelerated MAVRIC-SL with robust-PCA compared to conventional MAVRIC-SL in evaluation of total hip arthroplasties. Skeletal Radiol 51: 549-556, 2022.
23. Yang R, Liu C, Li L, Chen L, Liu WV and Zha Y: 3-T MRI in patients who received anterior cervical discectomy and fusion surgery with MAVRIC SL IR sequence: A feasibility study. Comb Chem High Throughput Screen 25: 1024-1030, 2022.
24. Park M, Moon Y, Han SH, Kim HK and Moon WJ: Myelin loss in white matter hyperintensities and normal-appearing white matter of cognitively impaired patients: A quantitative synthetic magnetic resonance imaging study. Eur Radiol 29: 4914-4921, 2019.
25. Togashi K, Nishimura K, Itoh K, Fujisawa I, Sago T, Minami S, Nakano Y, Itoh H, Torizuka K and Ozasa H: Ovarian cystic teratomas: MR imaging. Radiology 162: 669-673, 1987.
26. Lee SM, Choi YH, Cheon JE, Kim IO, Cho SH, Kim WH, Kim HJ, Cho HH, You SK, Park SH and Hwang MJ: Image quality at synthetic brain magnetic resonance imaging in children. Pediatr Radiol 47: 1638-1647, 2017.